Journal of Physics and Chemistry of Solids 121 (2018) 386–395

Contents lists available at ScienceDirect

Journal of Physics and Chemistry of Solids

journal homepage: www.elsevier.com/locate/jpcs

Adsorption of *Ne* on a planar solid *Mg* surface revisited

Leszek Szybisz[a,b,c,1], Salvador A. Sartarelli[d], Ignacio Urrutia[a,b,*]

[a] Departamento de Física, Centro Atómico Constituyentes, CNEA, Av. Gral. Paz 1499, RA–1650, Pcia, de Buenos Aires, Argentina
[b] Consejo Nacional de Investigaciones Científicas y Técnicas, Av. Rivadavia 1917, RA–1033AAJ Buenos Aires, Argentina
[c] Departamento de Física, Facultad de Ciencias Exactas y Naturales, Universidad de Buenos Aires, Ciudad Universitaria, RA–1428 Buenos Aires, Argentina
[d] Instituto de Desarrollo Humano, Universidad Nacional de General Sarmiento, Gutierrez 1150, RA–1663 San Miguel, Argentina

A B S T R A C T

In this study, we reexamined the wetting behavior of *Ne* adsorbed on a solid *Mg* surface. In a recent study, Zhou and Zhang (*J. Phys. Chem. Solids*, 2017, **103**, 123) reported an investigation of this system. They proposed an adsorption potential, $\phi_{ext}(z)$, and studied this system based on augmented density functional theory (DFT) to determine the wetting temperature T_w and critical prewetting temperature T_{cpw}. The value obtained for T_{cpw} differed greatly from that produced by Grand Canonical Monte Carlo simulations (*Phys. Rev. E*, 1999, **59**, 864) and previous DFT calculations (*Phys. Rev. E*, 2009, **79**, 011603). In the present study, we calculated the adsorption isotherms with the Kierlik–Rosinberg DFT for two different external potentials, i.e., the aforementioned $\phi_{ext}(z)$ and the proposed *ab initio* Chizmeshya–Cole–Zaremba (CCZ) potential. This study had two main aims. First, we aimed to identify the main sources of the discrepancies between the results obtained by Zhou and Zhang and those produced in other studies. Second, we analyzed the new data computed with the CCZ potential by applying the so-called arc-length continuation method. The new results supported the old ones, yielding more accurate values for both characteristic temperatures and indicating interesting new features of the system. We developed a novel alternative procedure for determining an appropriate value of T_{cpw} for moderately strong adsorbers. Assuming that *Ne* is liquid in the range of $T_w \leq T < T_t$, then the DFT calculations were extended into this region. We showed that close to T_t and after the prewetting jump, the growth of the films exhibited a sequence of layering transitions, which originated coalescent prewetting lines.

1. Introduction

Studying the physisorption of fluids on solid walls has attracted considerable interest over recent decades [1,2]. In the presence of solid substrates, fluids develop interfaces that exhibit a variety of features such as drying, critical wetting, prewetting (PW), wetting, layer formation, spreading, and filling. A volume containing reviews and discussions of theoretical and experimental investigations of this subject was published recently [3]. The most recent reports include those by Refs. [4,5]. Understanding the phase behavior of this type of system is fundamental for testing theoretical microscopic models and for devising practical applications in domains ranging from oil recovery to biology.

In this study, we consider a system where a liquid phase (l) is adsorbed on solid substrates (s) in the presence of a vapor atmosphere (v). Both fluid phases, i.e., the bulk liquid l and vapor v, coexist at temperature T when the chemical potential μ and the pressure P equal the corresponding saturation values $\mu_0(T)$ and $P_0(T)$, respectively. The latter quantities define $l-v$ coexistence lines in the $\mu-T$ and $P-T$ planes for temperatures that range from the triple point T_t to the critical point T_c. It is usually assumed that in the case of planar symmetry where flat inert walls exhibit an infinite extent in the x and y directions, the potential for the solid–fluid interaction $U_{sf}(z)$ is a function of the distance perpendicular to the surface, z, and the density profile of the adsorbed fluid depends only on this coordinate, i.e., $\rho(\mathbf{r}) = \rho(z)$.

A systematic classification of the adsorption on attractive planar surfaces was performed by Pandit, Schick, and Wortis [6]. The behavior of these systems depends on the strength of the fluid–fluid (*f-f*) attraction, ε_{ff}, the well depth of the substrate–fluid (*s-f*) interaction, $\mathscr{W}_{sf}$, the range of interactions, the temperature, T, and the chemical potential, μ. However, for long range adsorption potentials, the wetting properties are mainly determined by the ratio of the well depths $\varepsilon_r = \mathscr{W}_{sf}/\varepsilon_{ff}$ [6–9]. Given a value of ε_r, the results can be summarized as a phase diagram in the (T, μ) plane. For moderate substrates (i.e., when ε_r is slightly bigger than one), there is a first-order wetting transition at the point $[T_w, \mu_w]$ between the triple point temperature, T_t, and the critical point temperature, T_c. In this case T_w is characterized by the appearance of

* Corresponding author. Departamento de Física, Centro Atómico Constituyentes, CNEA, Av. Gral. Paz 1499, RA–1650, Pcia, de Buenos Aires, Argentina.
E-mail address: iurrutia@cnea.gov.ar (I. Urrutia).
[1] Deceased author.

https://doi.org/10.1016/j.jpcs.2018.05.016
Received 6 November 2017; Received in revised form 10 May 2018; Accepted 11 May 2018

coexisting microscopically thin and macroscopically thick adsorbed fluid films, whereas for $T < T_w$, the coverage of the adsorbed films is finite (incomplete wetting). Under these conditions, for $T \geq T_w$, there is an associated prewetting (PW) line, which extends away from $[T_w, \mu_w]$ into the region of pressures below the corresponding bulk saturation value $P_0(T)$. The locus of this line in the plane (T, μ) is determined by $\mu_{pw}(T) = \mu_0(T) + \Delta\mu_{pw}(T)$. A schematic phase diagram is depicted in Fig. 3 of [6], which show that the line of the transitions terminates at a surface critical prewetting (CPW) point $[T_{cpw}, \mu_{cpw}]$. The pioneering density functional theory (DFT) calculation of this phenomenon was reported by Ebner and Saam [10] in the case of *Ar* adsorbed on a CO_2 substrate. A PW transition is marked by a jump in the excess surface density (coverage), which is often expressed in nominal layers ℓ as

$$\Gamma_\ell = \frac{1}{[\rho_l(T)]^{2/3}} \int_0^\infty dz\,[\rho(z) - \rho_B]\,, \tag{1}$$

where $\rho(z)$ is the density profile, $\rho_B = \rho(z = \infty)$ is the asymptotic bulk density, which is usually the vapor at saturation $\rho_v(T)$, and $\rho_l(T)$ is the liquid density at bulk coexistence. The discontinuity in Γ_ℓ vanishes at T_{cpw}, where the coexisting thin and thick films become identical. For $T > T_{cpw}$, the adsorbed stable film grows continuously with increasing coverage. When the strength of attractive substrates is increased, the phase diagram contains several coalescent PW lines, as shown in Fig. 9. In the case of very strong substrates, the coverage increases from zero either continuously or in monolayer steps. In the latter case, each step is a first-order phase transition and each terminates in a critical point.

First-order surface phase transitions have been measured extensively for ^4He adsorbed on alkali-metal substrates (a survey of previous studies was given by Ref. [11]). The PW transitions of H_2 films on *Rb* and *Cs* have also been observed [12–14].

Recently, Zhou and Zhang [15] reported a study of the adsorption of *Ne* on a planar surface of the alkaline-earth metal *Mg*. The ratio ε_r for this system is about 3, as shown in Table 1, thereby indicating a moderately strong substrate. Hence, we may expect that T_w will be close to $T_t = 24.55$ K for *Ne*. No experimental results are available for *Ne/Mg*, so it would be interesting to produce reliable theoretical predictions of its wetting properties. For the calculations performed by Ref. [15], an adsorption potential $U_{sf}(z) = \phi_{ext}(z)$ was used in the framework of the augmented DFT devised by Zhou [16]. They reported a series of adsorption isotherms, which were used to determine $T_w = 23.82$ K, where this is slightly lower than T_t, and $T_{cpw} = 25.09$ K. Both results are listed in Table 1. Zhou and Zhang [15] compared their findings with the results obtained by Bojan et al. and Curtarolo et al. [8,17] based on Grand Canonical Monte Carlo (GCMC) simulations for a S10-4 adsorption potential, i.e., $U_{sf}(z) = U_{S10-4}(z)$, which are also shown in Table 1. The results determined for T_w by Zhou and Zhang [15] and Bojan et al. [8,17] are consistent, but that for T_{cpw} is quite different, thereby suggesting that the corresponding adsorption isotherms as a function of T should also be different. However, Zhou and Zhang overlooked a study by Sartarelli et al. [9] who analyzed the *Ne/Mg* system by applying DFT combined with an *ab initio* potential developed by Chizmeshya, Cole, and Zaremba (CCZ) [18], i.e., $U_{sf}(z) = U_{CCZ}(z)$. Importantly, the GCMC simulations [8,17] and DFT calculations reported by Sartarelli et al. [9] provide compatible values for both T_w and T_{cpw}, as shown in Table 1. The latter temperature is an important feature of wetting properties [10], so the aim of the present study was to revisit this system in order to clarify the situation.

The remainder of this paper is organized as follows. The formalism of a DFT for classical fluids is summarized in Section II, where we also compare the adsorption potentials for the *Ne/Mg* system. The wetting behavior results are described and discussed in Section III. Finally, we give our concluding remarks in Section IV.

2. Theoretical formalism

First, we outline the main features of DFT and, second, the adsorption potentials used in the previous studies by Refs. [8,9,15,17] are given.

2.1. DFT

The DFT is based on the existence of a grand canonical functional $\Omega(T, \mu, [\rho(\mathbf{r})])$ of the one-particle density $\rho(\mathbf{r})$, which depends parametrically on the two thermodynamic variables T and μ [19]

$$\Omega(T, \mu, [\rho(\mathbf{r})]) = \nu_{\rm id}\, k_B\, T \int d\mathbf{r}\, \rho(\mathbf{r}) \{\ln[\Lambda^3 \rho(\mathbf{r})] - 1\} + \mathcal{F}_{\rm DF}(T, [\rho(\mathbf{r})]) + \int d\mathbf{r}\, \rho(\mathbf{r})\, [U_{sf}(\mathbf{r}) - \mu]. \tag{2}$$

The first term is the ideal gas free energy, where k_B is the Boltzmann constant and Λ is the de Broglie thermal wavelength. The factor $\nu_{\rm id}$ is a free empirical parameter introduced by Ref. [20] to account for some quantum effects present in a *Ne* fluid as mentioned by Ref. [21] (in practice, it deviates slightly from unity, which corresponds to an ideal gas). The second term, $\mathcal{F}_{\rm DF}$, is the density functional for the excess

Table 1
Wetting properties of *Ne* adsorbed on *Mg*. The $\mathscr{W}_{sf}/\varepsilon_{ff}$ ratio, wetting T_w, and prewetting critical T_{cpw} temperatures are shown.

$\varepsilon_r = \frac{\mathscr{W}_{MgNe}}{\varepsilon_{NeNe}}$	U_{sf}	T_w	a_{pw}/k_B	T_{cpw}	$T_{cpw} - T_w$	Ref.
		[K]	[$K^{-1/2}$]	[K]	[K]	
2.79	U_{CCZ}	26				SM [18]
2.99[a]	U_{CCZ}	24				SM CW[b]
3.10	ϕ_{ext}	30				SM CW
2.77	U_{S10-4}	22±1		30.6[c]	8.6	GCMC [8,17]
2.79	U_{CCZ}	20.5	− 0.26	30[c]	9.5	DFT [9]
3.10	ϕ_{ext}	23.82		25.09	1.3	DFT [15]
2.99[a]	U_{CCZ}	20.8 ± 0.4[d]	− 0.28 ± 0.03[d]	29.23 ± 0.03	8.4	DFT CW
	U_{CCZ}	21.0 ± 0.1[e]	− 0.31 ± 0.01[e]	29.23 ± 0.03	8.2	DFT CW

[a] This value corresponds to $\varepsilon_{NeNe}(T = T_t) = 31.66$ K.
[b] CW denotes the current work.
[c] These values are the upper limit for critical prewetting temperature.
[d] Data for $T \geq T_t$ were fitted.
[e] Data for $T \geq 22$ K were fitted.

Helmholtz free energy for the *f–f* interaction. The third term comprises the contribution due to the external adsorption potential and the chemical potential at equilibrium.

The quantity $\mathcal{F}_{\rm DF}$ is usually decomposed into one reference term, $\mathcal{F}_{ref}$, and one perturbation term, $\mathcal{F}_{per}$ (see Ref. [19])

$$\mathcal{F}_{\rm DF}(T,[\rho(\mathbf{r})]) = \mathcal{F}_{ref}(T,[\rho(\mathbf{r})]) + \mathcal{F}_{per}(T,[\rho(\mathbf{r})]) = \int d\mathbf{r}\,\rho(\mathbf{r})\,\Delta f_{\rm HS}[\bar{\rho}(\mathbf{r});d_{\rm HS}]\Big] + \frac{1}{2}\iint d\mathbf{r}\,d\mathbf{r}'\rho(\mathbf{r})\,\rho(\mathbf{r}')\Phi_{\rm per}(|\mathbf{r}-\mathbf{r}'|). \tag{3}$$

The reference term is repulsive and it is approximated by a hard-sphere (HS) fundamental measure theory (FMT) functional described by Kierlik and Rosinberg (KR) [22], which has proved very successful even in highly inhomogeneous situations. The KR version is completely equivalent to the original FMT formulated by Rosenfeld [23]. $d_{\rm HS}$ is the HS diameter. The perturbation contribution $\Phi_{\rm per}(|\mathbf{r}-\mathbf{r}'|)$ is currently assumed as the mean-field approximation (MFA) of the attractive part of the *f–f* interaction given by the spherically symmetric Lennard-Jones (LJ) 12–6 potential as introduced by Weeks, Chandler, and Andersen (WCA) [24].

$$\Phi_{\rm per}^{\rm WCA}(r) = \begin{cases} -\tilde{\varepsilon}_{ff}\,, & r \le r_{min} \\ 4\tilde{\varepsilon}_{ff}\left[\left(\frac{\tilde{\sigma}_{ff}}{r}\right)^{12} - \left(\frac{\tilde{\sigma}_{ff}}{r}\right)^{6}\right], & r > r_{min} \end{cases} \tag{4}$$

where $r = |\mathbf{r}-\mathbf{r}'|$ and $r_{min} = 2^{1/6}\tilde{\sigma}_{ff}$ is the position of the LJ minimum. It should be noted that in several older studies (e.g. [20,25]), the function $\Phi_{\rm per}(r)$ was approximated by the method proposed by Bruno et al. given as Eq. (17) in Ref. [26]. However, as shown by Sartarelli et al. [9], this approach produces diverging unphysical oscillations in the density profiles for temperatures close to T_t. The strength and size parameters, $\tilde{\varepsilon}_{ff}$ and $\tilde{\sigma}_{ff}$, are assumed to be functions of T, as suggested previously by Refs. [20,25].

Since μ is constant along the entire adsorbed fluid, so for a planar symmetry, the last integral in Eq. (2) gives

$$\int d\mathbf{r}\,\rho(\mathbf{r})\,\mu = \mu\,A\int_0^\infty dz\rho(z) = \mu\,N, \tag{5}$$

where A is the surface area of the substrate and N is the number of adsorbed particles. Then, the excess of adsorbed atoms per unit area may be evaluated with

$$\frac{N_{exc}}{A} = \int_0^\infty dz\,[\rho(z)-\rho_B]. \tag{6}$$

In fact, the coverage defined in Eq. (1) is a dimensionless version of this quantity.

Different improvements have been proposed for the DFT over time for both contributions, i.e., the reference repulsive term and the attractive term (e.g., see comments by Hansen-Goos [27]). Thus, in the FMT functional of HS, a tensorial correction was introduced by Tarazona [28] to avoid free energy divergences when $\rho(\mathbf{r})$ becomes highly peaked, where it correctly describes both the HS crystal and the fluid in extreme confinement. In the case of the system examined in the present study with $\varepsilon_r \approx 3$, the density $\rho(\mathbf{r})$ does not exhibit very pronounced peaks, and thus the tensorial term is not necessary. Pronounced peaks are typical of stronger substrates, e.g. they are found for *Ne/Gr*, which corresponds to $\varepsilon_r \approx 9$ (see Table V in Ref. [21]). In addition, modifications were proposed for the perturbative contribution term based on changes to the MFA of the attractive part of the f–f interaction. For instance, in order to obtain accurate bulk properties for the LJ fluid, Peng and Yu [29] introduced a perturbative MFA-attractive term in their DFT based on the modified Benedict–Webb–Rubin equation of state given by Johnson et al. [30]. In this DFT, the attractive contribution to the excess free energy per particle contains 14 coefficients, which are functions of T (these coefficients contain 32 adjustable linear parameters, which are listed in Table 10 of the study by Johnson et al. cited above). In the present study, instead of using a MFA-attractive term based on an equation of state with many free coefficients, the strength and size parameters, $\tilde{\varepsilon}_{ff}$ and $\tilde{\sigma}_{ff}$, of the LJ potential are fitted. It should be noted that the temperature dependence of $\varepsilon(T)$ and $\sigma(T)$ was assumed in many previous studies that dealt with thermophysical properties (e.g., see Refs. [31–33] and the citations therein). It has been shown that the current semi-empirical density functional for *Ne/Mg* captures the relevant properties of the bulk *Ne* and liquid–vapor interface [9] with sufficient accuracy.

2.2. Adsorption potentials

Next, we describe the physisorption potentials utilized in previous studies [8,9,15,17]. As mentioned above, the adsorption potential $\phi_{ext}(z)$ employed by Zhou and Zhang was constructed *ad hoc*. According to the description provided by Ref. [15], the values of the potential between a *Ne* atom and *Mg* surface calculated by quantum DFT were fitted into $\phi_{ext}(z)$ generated from a truncated and shifted (at $z = z_{cs}$) $\phi_{fitting}(z)$ comprising a repulsive inverse power law and an attractive Yukawa potential:

$$\phi_{ext}(z) = \begin{cases} \phi_{fitting}(z) - \phi_{fitting}(z_{cs})\,, & z \le z_{cs} \\ 0\,, & z > z_{cs}\,. \end{cases} \tag{7}$$

$$\phi_{fitting}(z) = 4\,\varepsilon_{inv}\left(\frac{\sigma_{Mg-Ne}}{z}\right) + \varepsilon_{Yuk}\exp[-\kappa(z/\sigma_{Mg-Ne})]/(z/\sigma_{Mg-Ne})\,. \tag{8}$$

The values of the four fitting parameters were $\varepsilon_{inv}/k_B = 112.7$ K, $\sigma_{Mg-Ne} = 0.2652$ nm, $n = 3.1341$, and $\varepsilon_{Yuk}/k_B = -544.0$ K, and the truncating distance for $\phi_{fitting}(z)$ was set as $z_{cs} = 0.7967$ nm. This potential was shown in Fig. 1 given by Ref. [15], where it was compared with $U_{CCZ}(z)$. The latter potential was only utilized in the study reported by Ref. [9], so it is convenient to write its expression as

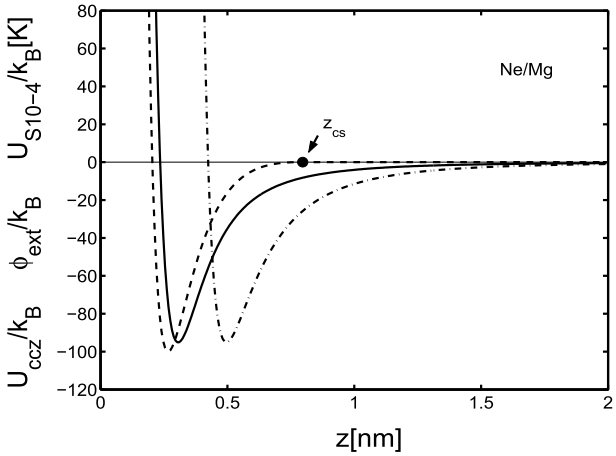

Fig. 1. Comparison of the adsorption potentials for the *Ne/Mg* system. The solid, dashed, and dash-dotted curves correspond to the U_{CCZ}, ϕ_{ext}, and U_{S10-4} potentials, respectively. z_{cs} indicates the truncating distance for $\phi_{ext}(z)$ (see text).

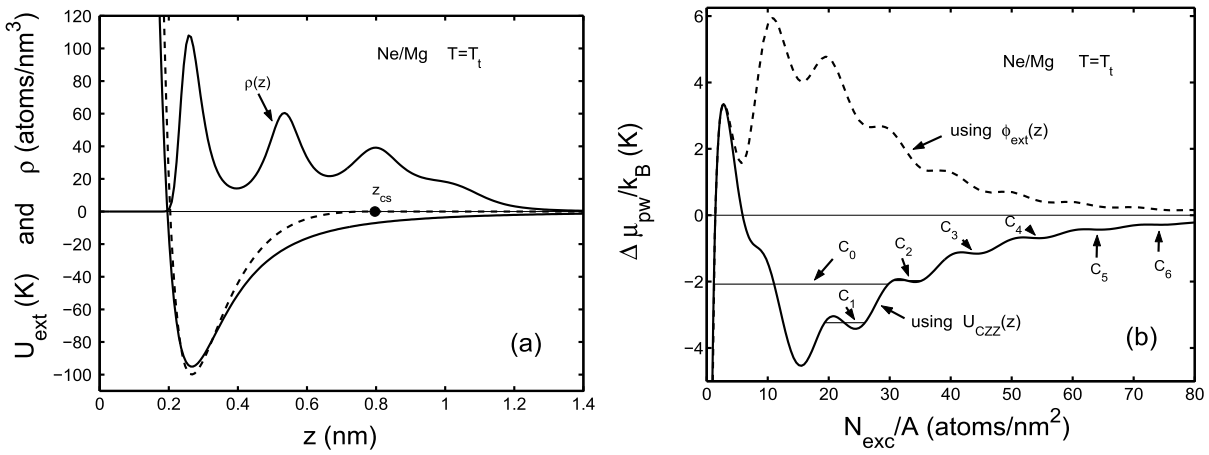

Fig. 2. (a) The three-peak density profile of a film corresponding to $N_{exc}/A = 30$ atoms/nm^2 at $T = T_t = 24.55$ K, calculated in the present study with the $\phi_{ext}(z)$ potential. The dashed and solid curves are the $\phi_{ext}(z)$ and $U_{CCZ}(z)$ potentials, respectively. The positions of the minima coincide for both potentials because U_{CCZ} was shifted. (b) Adsorption isotherms for the *Ne/Mg* system at $T = T_t$ calculated using the DFT given by Ref. [9]. The solid and dashed curves were evaluated with the $U_{CCZ}(z)$ and $\phi_{ext}(z)$ potentials, respectively. Horizontal lines indicate coverage jumps, where that denoted by C_0 contributes to the main PW line, and the meanings of C_1, C_2, …, C_6 are given in the text.

given by Ref. [18]:

$$U_{CCZ}(z) = V_0(1 + \alpha z)e^{-\alpha z} - f\left[(z - z_{vdW})\beta(z - z_{vdW})\right]\frac{C_{vdW}}{(z - z_{vdW})^3}\,, \tag{9}$$

where

$$f(\xi) = 1 - e^{-\xi}\left(1 + \xi + \frac{\xi^2}{2}\right), \tag{10}$$

and

$$\beta(\zeta) = \frac{\alpha^2\zeta}{(1 + \alpha\zeta)}\,. \tag{11}$$

The first term in Eq. (9) is the Hartree–Fock repulsive energy and the second term is the attractive van der Waals (vdW) contribution to the interaction. C_{vdW} and z_{vdW} are the strength and position of the vdW potential, respectively. The dumping function $f(\xi)$ accounts for the atom-substrate wave function overlap and the function $\beta(\zeta)$ overcomes the unphysical divergence at $z = z_{vdW}$ [18,34]. For $z \gg z_{vdW}$ this attractive contribution leads to the term $-C_3/z^3$ of the well known 9–3 potential introduced by Ricca [35]. The parameters corresponding to the *Ne/Mg* system $V_0 = 1.774$ eV, $\alpha = 1.347$ a$_0^{-1}$ (with a$_0 = 0.0529$ nm), $C_{vdW} = 2.130$ eV-a$_0^3$, and $z_{vdW} = 0.624$ a$_0$ were taken from Table 1 given by Ref. [18]. The ϕ_{ext} and U_{CCZ} potentials are shown in Fig. 1.

In addition, the potential $U_{S10-4}(z)$ utilized in the GCMC simulations represents the LJ interaction of adsorbate atoms in the solid, that are located on successive planes parallel to the surface [36]. If the interplanar spacing is d, then the potential as a function of the perpendicular distance of a fluid atom from the surface z can be written as

$$U_{S10-4}(z) = \varepsilon_{1s}\sum_{j=0}^{3}\left[\frac{2}{3}\left(\frac{\sigma_{gs}}{z + jd}\right)^{10} - \frac{5}{3}\left(\frac{\sigma_{gs}}{z + jd}\right)^{4}\right] \tag{12}$$

where small corrections for the interactions between adsorbate atoms and the more distant planes ($j > 3$) are neglected. ε_{1s} is the strength of the interaction and σ_{gs} is the size parameter for the potential. Bojan et al. [17] used values of $d = 0.401$ nm and $\sigma_{gs} = 0.501$ nm. Under these conditions, the relationship between the well depth, $\mathscr{W}_{sf}$, for the interaction of an atom with the entire surface and ε_{1s}, is $\mathscr{W}_{sf} \approx 1.2\,\varepsilon_{1s}$. A value of $\mathscr{W}_{sf}/k_B = 95$ K was assumed for the *Ne/Mg* system. This U_{S10-4} potential is also plotted in Fig. 1, which shows that it exhibits a tail similar to that of $U_{CCZ}(z)$.

3. Analysis of wetting properties

After outlining the main features of the DFT and the three adsorption potentials for *Ne/Mg*, before discussing results for wetting

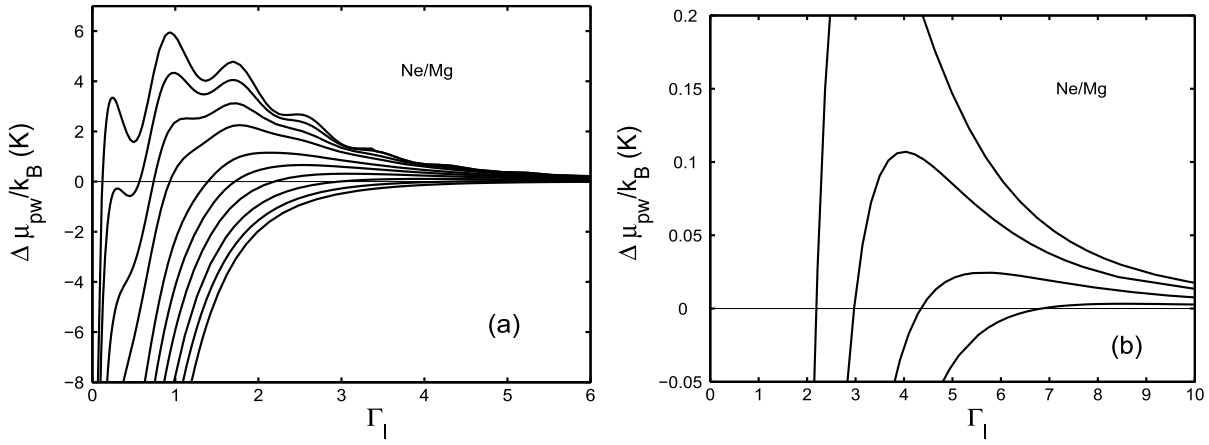

Fig. 3. (a) Adsorption isotherms $\Delta\mu_{pw}(T)$ for the *Ne/Mg* system obtained with the $\phi_{ext}(z)$ potential. From bottom to top the results correspond to temperatures of $T = 43,41,39,37,35,33,30,28,26$, and 24.55 K. (b) Enlarged image of the adsorption isotherms at temperatures of $T = 43,41,39$, and 37 K.

properties, we note the differences between the assumptions made in the calculations conducted by Refs. [15] and [9]. As the reference term of the Helmholtz free energy, Zhou and Zhang [15] utilized a formalism developed by one of them [16], which is a version of the KR FMT [22] augmented by introducing the Mansoori–Carnahan–Starling–Leland (MCSL) [37] bulk equation of state. The original KR FMT was utilized for the calculations reported by Ref. [9]. This original formalism corresponds to the Carnahan–Starling (CS) [38] bulk equation of state. In practice, the MCSL bulk equation of state is more suitable for studying binary mixtures, but in the case of a one-component HS fluid, the difference due to the CS approach is negligible, as shown in Fig. 3 given by Ref. [39]. The same MFA given by Eq. (4) was used for the perturbation term by both [15] and [9]. The differences are that the calculations performed by Zhou and Zhang used the same values for ε_{Ne-Ne} and σ_{Ne-Ne} at all temperatures and the LJ potential was truncated at $4\sigma_{Ne-Ne}$, whereas in our calculations, we assumed that the LJ parameters are functions of T and the LJ potential is not truncated. In our DFT, the effective strength and size parameters, $\tilde{\varepsilon}_{Ne-Ne}(T)$ and $\tilde{\sigma}_{Ne-Ne}(T)$, as well as ν_{id} were fitted to data from the liquid–vapor coexistence curve shown in Table III given by Ref. [40].

For the $\phi_{ext}(z)$ and $U_{CCZ}(z)$ adsorption potentials, Zhou and Zhang stated that have very similar attractive well shapes, except that $\phi_{ext}(z)$ is slightly deeper than $U_{CCZ}(z)$ and the equilibrium distances are also slightly different, i.e., $z_{min} = 0.268$ nm and $z_{min} = 0.307$ nm, respectively. Based on these features, they claimed that "*these differences should certainly not affect the predictions of the wetting properties*." However, there is an additional very important difference because $\phi_{ext}(z)$ finishes suddenly in a short range at $z_{cs} = 0.7967$ nm, whereas $U_{CCZ}(z)$ exhibits a long range tail that is proportional to $-1/z^3$. Undoubtedly, the range of the adsorption potential affects the energetics of the adsorbed film. In addition, although the $U_{S10-4}(z)$ potential has its minimum at $z_{min} = 0.497$ nm, i.e., it is shifted by about 0.2 nm with respect to the other two, its curve shape is similar to that of $U_{CCZ}(z)$ and it has the same depth. In fact, these $U_{CCZ}(z)$ and $U_{S10-4}(z)$ potentials are very similar to those for the *Ne/Li* system shown in Fig. 3 given by Ref. [9].

As mentioned in the introduction, Zhou and Zhang [15] determined the wetting and CPW temperatures listed in Table 1 as $T_w = 23.82$ K and $T_{cpw} = 25.09$ K, respectively. This value of T_w is slightly lower than the triple point temperature of *Ne* and it is similar to that obtained in other studies [8,17] and [9], which are also quoted in Table 1. However, $T_{cpw} = 25.09$ K yields a difference of $T_{cpw} - T_w = 1.3$ K, much smaller than the values of 8.6 and 9.5 K determined by Refs. [17] [8], and [9], respectively. This suggests that the energetics calculated by Zhou and Zhang differ from those evaluated in the other two studies. Therefore, in the remainder of this section, we present a reanalysis of the *Ne/Mg* system to identify possible explanations for this discrepancy.

In Fig. 5b of their study [15], Zhou and Zhang showed that according to their calculations, $\rho(z)$ for $N_{exc}/A = 30.09$ atoms/nm^2 corresponds to the thicker film at the PW point for $T = 24.50$ K. This density profile exhibits three peaks. In order to facilitate the analysis, the density profile for $N_{exc}/A = 30$ atoms/nm^2 evaluated at T_t using the procedure describe by Ref. [9] and $\phi_{ext}(z)$ is shown in Fig. 2a together with the external potential. If we consider the structures of $\rho(z)$ and $\phi_{ext}(z)$, it is clear that the first peak is located at the minimum of the potential. The distance between the peaks should be approximately the diameter of a *Ne* atom $\sigma_{NeNe} \simeq 0.28$ nm, so we expect that the third peak should be located at about 0.56 nm from the minimum. For $\phi_{ext}(z)$, the difference between the truncating distance and the position of the minimum is $z_{cs} - z_{min} \simeq 0.53$ nm. Therefore, the third peak should be at approximately z_{cs}, as shown in Fig. 2a. Hence, this peak does not contribute to the negative energy given by the integral $\int dz\rho(z)\phi_{ext}(z)$. Fig. 2a also shows the $U_{CCZ}(z)$ potential, which was shifted so the minima of both potentials coincided. In the case of the latter potential, the entire third peak contributes to the integral $\int dz\rho(z)U_{CCZ}(z)$. Moreover, the second layer makes a more important contribution when combined with $U_{CCZ}(z)$ compared with that in the case of $\phi_{ext}(z)$. These facts explain an important difference between the energetics corresponding to both potentials. For instance, Fig. 2b shows the adsorption isotherms evaluated with the DFT describe by Ref. [9] in the cases of both potentials $\phi_{ext}(z)$ and $U_{CCZ}(z)$. The results only coincide in terms of $N_{exc}/A \leq 5$ atoms/nm^2 for the larger coverages $\Delta\mu_{pw}/k_B$ produced when the potential $\phi_{ext}(z)$ remains positive. In the limit of very thick films, $\Delta\mu_{pw}/k_B \to 0$ is obtained for both potentials, although this limit is reached from below for $U_{CCZ}(z)$ and from above for $\phi_{ext}(z)$, thereby leading to stable and unstable solutions for $\rho(z)$, respectively. Hence, according to our calculations, there is no wetting at the triple point temperature in the latter case.

For $\phi_{ext}(z)$, there is no wetting at T_t, so we applied a simple model (SM) to obtain an estimate of T_w for this potential. In the SM, one compare the energy cost of forming a thick film (surface tension) with the benefit due to the fluid-surface attractive interaction and the wetting condition expressed according to Eqs. (1) and (2) given by Ref. [18], that becomes

$$-[\rho_l(T) - \rho_v(T)]\int_{z_{\min}}^{\infty} dz\, U_{sf}(z) = [\rho_l(T) - \rho_v(T)]I_u \geq 2\,\gamma_{lv}(T), \tag{13}$$

where $\gamma_{lv}(T)$ is the liquid–vapor surface tension at saturation. In fact, instead of examining the wetting by simply inputting sets of densities $\rho_l(T)$ and $\rho_v(T)$ at coexistence and $\gamma_{lv}(T)$ into Eq. (13) in a similar manner to a black box, it is convenient to find an expression for T_w. Thus, the difference in the densities may be written according to the simple and accurate Guggenheim's form given as Eq. (6.4) by Ref. [41].

$$\rho_l(T) - \rho_v(T) = (7/2)\rho_c(1 - T/T_c)^{1/3}, \tag{14}$$

where $\rho_c = 14.43$ nm^{-3} is the bulk density at the critical point $T_c = 44.4$ K, and the liquid–vapor surface tension may be expressed based on the prediction from the fluctuation theory of critical phenomena (e.g., see Ref. [42])

$$\gamma_{lv}(T) = \gamma_{lv}^0(1 - T/T_c)^{5/4}, \tag{15}$$

where $\gamma_{lv}^0 = 1135$ K/nm^2. Thus, the wetting condition reduces to a condition for the integral I_u.

$$I_u \geq \frac{2\,\gamma_{lv}(T)}{\rho_l(T) - \rho_v(T)} = \frac{4\,\gamma_{lv}^0}{7\,\rho_c}\left(1 - \frac{T}{T_c}\right) \tag{16}$$

Hence, by inverting this relationship, we obtain

$$T_w(\mathrm{SM}) = \left[1 - \left(\frac{7\,\rho_c\,I_u}{4\,\gamma_{lv}^0}\right)^{12/11}\right]T_c. \tag{17}$$

By replacing the result for $I_u(U_{CCZ})$ in this equation, we obtain the value of $T_w(\mathrm{SM}) = 24$ K given in Table 1, which is slightly lower than that given by Ref. [18]. For $\phi_{ext}(z)$, we obtain $I_u = 14.5$ K·nm, so the wetting temperature becomes $T_w(\mathrm{SM}) = 30$ K, i.e., several degrees higher than T_t. Therefore, in order to determine T_w, the adsorption isotherms for $\phi_{ext}(z)$ were evaluated over the temperature range from T_t to T_c.

Fig. 3 shows the adsorption isotherms calculated using the DFT described by Ref. [9] and the $\phi_{ext}(z)$ potential. The results correspond to temperatures of $T = 24.55$, 26,28,30,33,35,37,39,41, and 43 K. These results suggest nonwetting because the limiting value $\Delta\mu_{pw} = 0$ is always reached from above, as found at T_t. This feature is shown clearly in the sub-plot in Fig. 3b, where finite adsorption can be observed even very close to T_c.

We recalculated the adsorption isotherms obtained with the DFT described by Ref. [9] by using the $U_{CCZ}(z)$ potential for temperatures in the range of $T = 24.55$, 25 in steps of 1 K–30 K, and obtained the results shown in Fig. 4a. Clearly, there is a dramatic difference between the results in Figs. 3a and 4a. In particular, in the latter case, the limiting value $\Delta\mu_{pw} = 0$ is always reached from below. The PW jumps Γ_ℓ *vs* $\Delta\mu_{pw}$ shown in Fig. 9 given by Ref. [9] were determined using Maxwell

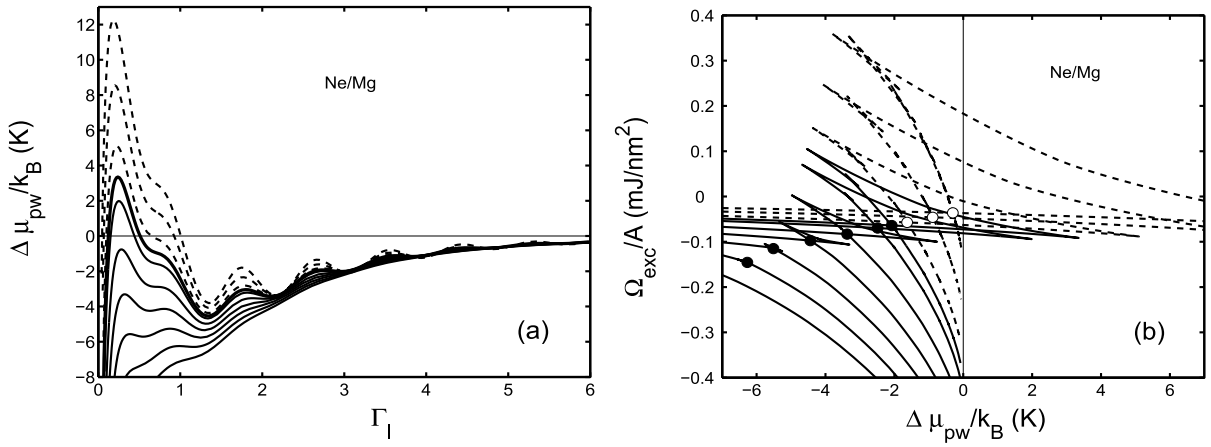

Fig. 4. (a) Adsorption isotherms $\Delta\mu_{pw}(T)$ for the *Ne/Mg* system obtained with the $U_{CCZ}(z)$ potential, from bottom to top the solid lines correspond to temperatures of T = 30,29,28,27,26,25, and 24.55 K, while the dashed lines correspond to T = 24,23, and 22 K. (b) Excess of the grand potential per unit area as a function of the reduced chemical potential for the same sequence of temperatures shown in (a), where the full and open circles indicate the loci of the main PW line. In both panels, the curves merge into the $\Delta\mu_{pw} = 0$ line for large coverages.

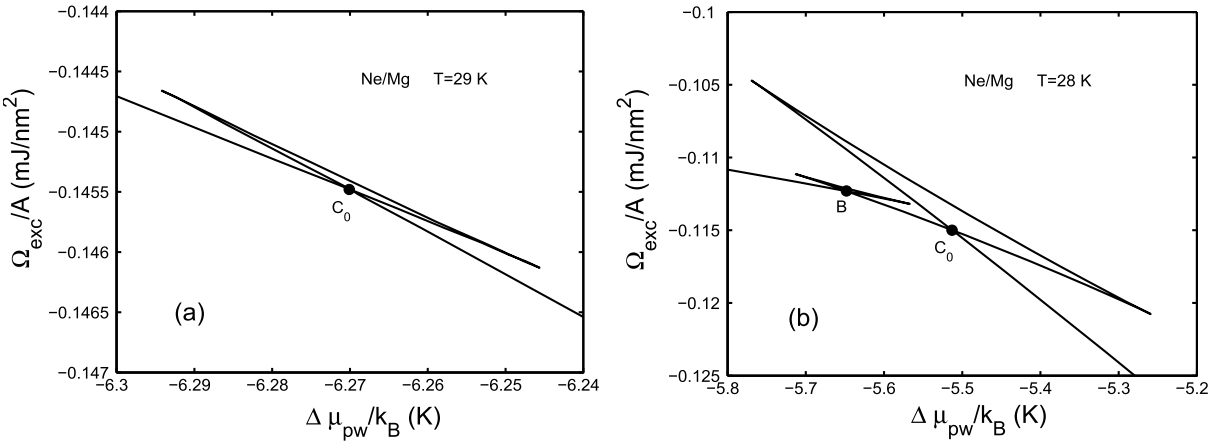

Fig. 5. Enlarged images of the energy curves shown in Fig. 4b for T = 29 and 28 K. The points denoted by C_0 in both sub-plots indicate the locus of the main PW line, and the meaning of point B in sub-plot (b) is explained in the text.

(equal area) constructions. By contrast, in the present study, the stable configurations at coverage jumps were determined by applying the so called arc-length continuation algorithm to trace the connected stable and metastable branches, which is based on the crossing of Ω_{exc}/A *vs* $\Delta\mu_{pw}$ lines (Ω_{exc} is the excess of grand potential). This procedure was also utilized by Zhou and Zhang. A detailed description of this method was given in our previous studies [43,44]. The results for the excess of the grand potential per unit area as a function of the reduced chemical potential are shown in Fig. 4b, where the circles depict the locus of the PW line. Fig. 4a indicates the continuous growth of stable films at T = 30 K and suggest a coverage jump at T = 29 K, which is not visible in Fig. 4b due to the scale of the drawing. In order to overcome this difficulty, the data corresponding to this temperature are plotted on an enlarged scale in Fig. 5a, where the crossing can be seen. Fig. 5b shows the energy data at T = 28 K on an enlarged scale, where two crossings can be observed clearly. Crossing C_0 lies on the main PW line and point B indicates the location of a first-order transition that occurred at small coverages. In fact, both these transitions may be inferred from the oscillations shown in Fig. 4a.

At lower temperatures, the adsorption isotherms exhibit interesting fine structures, which were not considered in our previous study [9]. For instance, the data corresponding to $T = T_t$ are plotted in Fig. 6. Fig. 6a shows that there are several crossing points. The crossing point denoted by C_0 lies on the main PW line, point C_1 corresponds to metastable films with small coverage, and the other C_i points correspond to the grow of thickness in layers, as mentioned in the Introduction for rather strongly attractive surfaces. The corresponding jumps in coverage are indicated by horizontal lines in Fig. 2b. In addition, the crossing C_6 is depicted in Fig. 6b. Similar features were also exhibited by the data obtained at T = 25 K.

3.1. Further analysis at T = 28 K

The adsorption at T = 28 K was examined in previous studies by Bojan et al. [17], Sartarelli et al. [9], and Zhou and Zhang [15]. Therefore, we specifically consider the behavior at this temperature. The adsorption isotherm evaluated in the present study as N_{exc}/A *vs* P is shown in Fig. 7. The coverage jumps denoted as C_0 and B are those identified in Fig. 5b. After these jumps, the thickness grows continuously while the pressure approaches the experimental value from below at liquid–vapor coexistence $P_0(T = 28\ \text{K}) = 1.304$ atm. We note that in the limit of very thick films, the densities of the liquid and vapor phases should approach their bulk values at coexistence. Fig. 8 shows the density profile of the very thick film with N_{exc}/A = 200 atoms/nm^2 calculated at T = 28 K. After the oscillations exhibited below $z \simeq 2.5$ nm, the liquid phase reaches a plateau with density $\rho_l = 35.47\ \text{nm}^{-3}$, and the asymptotic density of the vapor phase becomes $\rho_v = 0.37\ \text{nm}^{-3}$. Both these densities coincide with the corresponding experimental bulk

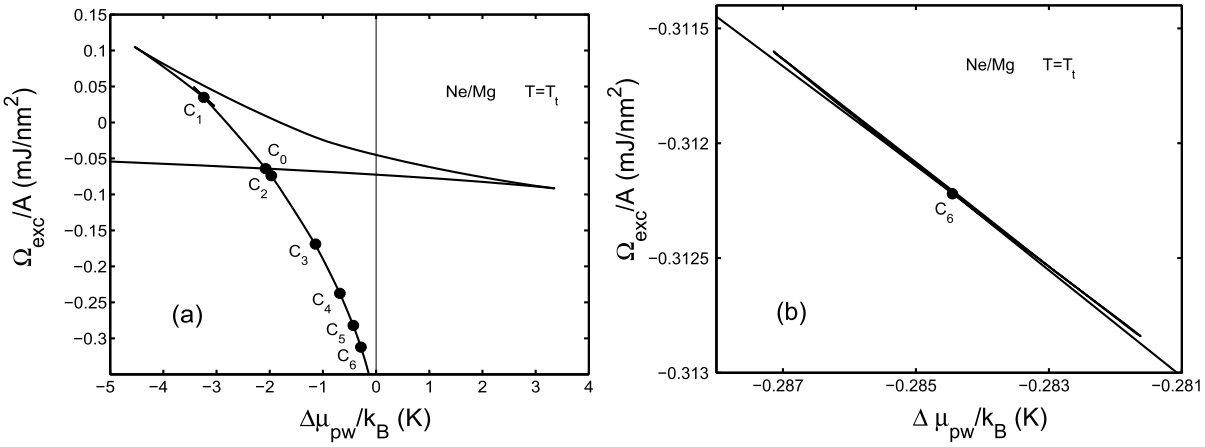

Fig. 6. (a) Enlarged image of the energy curve shown in Fig. 4b for $T = T_t = 24.55$ K. The point denoted by C_0 lies on the main PW line. The meanings of points C_1, C_2, …, C_6 are explained in the text. (b) Enlargement of the crossing C_6.

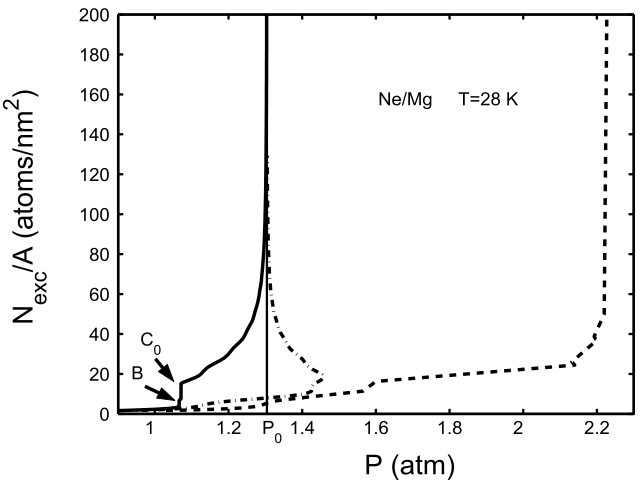

Fig. 7. Adsorption isotherms for the *Ne/Mg* system at $T = 28$ K as a function of pressure. The solid and dash-dotted curves were calculated in the present study using the $U_{CCZ}(z)$ and $\phi_{ext}(z)$ potentials, respectively. The dashed curve is a schematic representation of the results reported by Zhou and Zhang [15]. The experimental saturated vapor pressure at this temperature, $P_0 = 1.304$ atm, is indicated by the vertical line.

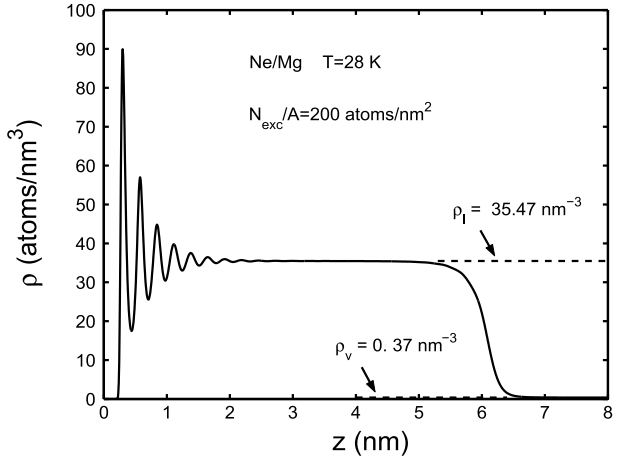

Fig. 8. Density profile of a very thick film of *Ne* adsorbed on *Mg* at $T = 28$ K obtained for the $U_{CCZ}(z)$ potential. The dashed and dash-dotted lines denote the liquid $\rho_l = 35.47$ nm^{-3} and vapor $\rho_v = 0.37$ nm^{-3} densities for coexistence at this temperature, respectively.

values at liquid–vapor coexistence, thereby supporting the accuracy of the current calculations. The dashed curve in Fig. 7 is a schematic representation of the adsorption isotherm shown in Fig. 2a given by Zhou and Zhang [15]. This curve indicates that the asymptotic pressure for very thick films $P_{asympt}(ZZ) = 2.227$ atm is much larger than the experimental saturated vapor pressure $P_0(T = 28\text{ K}) = 1.304$ atm. In order to demonstrate that this inconsistency is not caused by the $\phi_{ext}(z)$ potential, we evaluated the adsorption isotherm by using this potential within the framework of the DFT given by Ref. [9]. The results are also plotted in Fig. 7, which indicate that the pressure approaches the experimental saturation value from above. Moreover, in the case of $T = 24.50$ K, the asymptotic value of the pressure shown in Fig. 3c given by Ref. [15], $P_{asympt}(ZZ) = 0.67$ atm, is about 50% larger than the corresponding experimental value at vapor saturation $P_0(T = T_t) = 0.43$ atm. These results indicate that in the limit of very thick films, the augmented DFT version applied by Zhou and Zhang overestimates the asymptotic pressure, which should agree with $P_0(T)$.

3.2. Wetting temperatures

Next, we determined T_w from our new data. If the tail of the adsorption potential has the vdW form, i.e., $U_{sf}(z \to \text{large}) \approx -C/z^3$, then the tangency to the coexistence curve ($\Delta\mu_{pw} = 0$) is described by the following relationship [6,7].

$$\Delta\mu_{pw}(T) = a_{pw}\,(T - T_w)^{3/2}\,, \tag{18}$$

where a_{pw} is a model parameter [12]. For strong substrates, wetting may be observed at T_t or at even lower temperatures. The values of $\Delta\mu_{pw}$ corresponding to the bold points in Fig. 4b are shown as a function of T in Fig. 9. A nonlinear fit of these data to Eq. (18) yielded the results given in Table 1, and the dashed curve in Fig. 9 indicates the quality of the adjustment. The wetting temperature obtained, $T_w = 20.8 \pm 0.4$ K, which is lower than T_t, is in good agreement with the GCMC value $T_w = 22 \pm 1$ K quoted in Table 1 by Ref. [8].

Figs. 4 and 5 indicate that T_{cpw} lies between $T = 29$ and 30 K. In order to enlarge the set of data close to T_{cpw}, we evaluated the isotherms at $T = 27.5$, 28.5, and 29.5 K. The crossing points C_0 corresponding to $T = 27.5$ and 28.5 K are shown in Fig. 9, where these new data follow

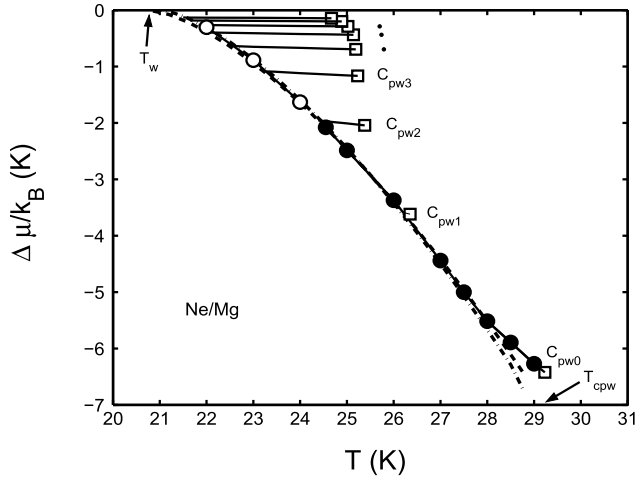

Fig. 9. Full circles denote the reduced chemical potential as a function of temperature along the main PW line for $T \geq T_t$ and open circles are data for $T < T_t$. The dashed curve shows the fit of the data for $T \geq T_t$ when used to determine T_w, and the dot-dashed curve is the fit for all the data. Solid curves represent the sequence of i-th PW lines and squares indicate their critical points C_{pwi}.

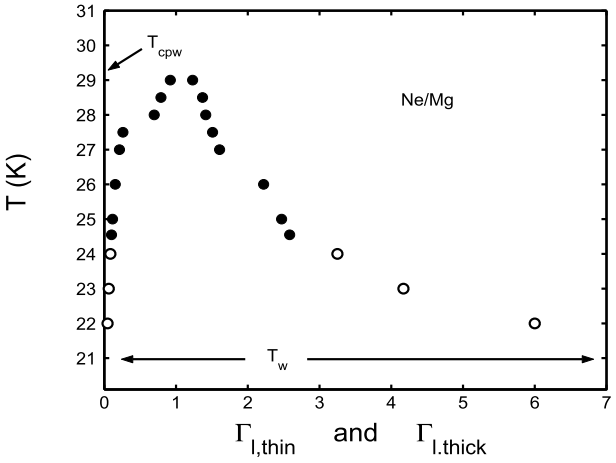

Fig. 10. Coverage of coexisting thin and thick films along the main PW line as a function of temperature.

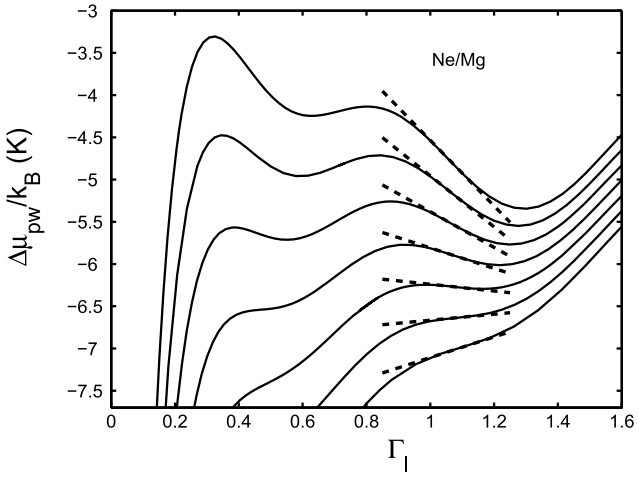

Fig. 11. Adsorption isotherms for coverages close to the main PW regime, where from the bottom to the top, they correspond to T = 30,29.5, 29,28.5, 28,27.5, and 27 K. Dashed straight lines indicate the slopes used for determining T_{cpw}.

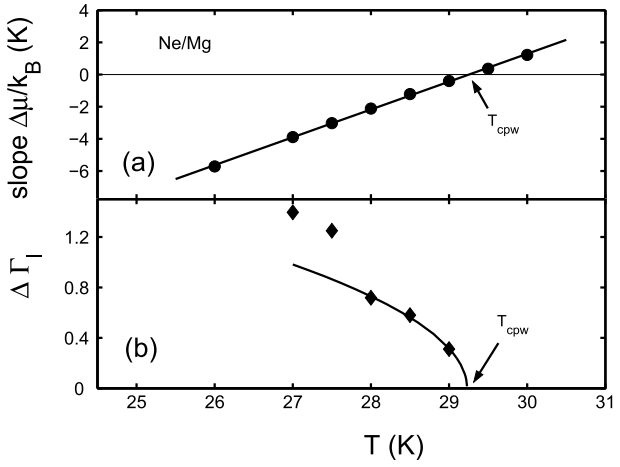

Fig. 12. (a) Slope of the reduced chemical potential shown in Fig. 11 as a function of temperature. The solid straight line represent the fit of the data used for determining T_{cpw}. (b) Coverage jump along the main PW line as a function of temperature. The solid curve was evaluated with Eq. (19).

the trend of the initial series perfectly. The evolution of the PW phenomenon characterized by the jump in coverage $\Delta\Gamma_\ell = \Gamma_{\ell,thick} - \Gamma_{\ell,thin}$ at $\Delta\mu_{pw}(T)$ can be observed in Fig. 10. The largest jump occurs close to T_w, but it then shrinks as T increases, and eventually disappears at T_{cpw} where the thin and thick films merge. Thus, $\Delta\Gamma_\ell$ serves as an order parameter that vanishes at the CPW point [10]. However, using data based on the coverages of adsorbed critical films for estimating T_{cpw} in the case of a relatively strong attractive substrate such as *Mg* presents problems. More than one loop develops for temperatures in T < 28.5 K, so its evolution with temperature is not smooth (e.g., see Figs. X and Vb). To overcome this problem, we studied the dependence of the slope of the isotherm on T at the point where it changed concavity at the PW well. The data plotted in Fig. 11 indicate that this point is near Γ_ℓ = 1.1. Fig. 12a shows that this slope is a smooth function of temperature and it becomes zero at T_{cpw}. The behavior of this slope is linear and it can be evaluated beyond T_{cpw}, so this critical temperature can be determined precisely. A linear fit yielded T_{cpw} = 29.23 ± 0.03 K, as shown in Table 1, and the quality of the fit is depicted in Fig. 12a. Using this value of T_{cpw}, we checked the asymptotic behavior

$$\Delta\Gamma_\ell(T) = b_{pw}(T_{cpw} - T)^{1/2}\,, \tag{19}$$

that is expected under the MFA used in the present study for the attractive *f-f* interaction [45]. Fig. 12b shows that this equation is satisfied for temperatures very close to T_{cpw} when b_{pw} = 0.658 $K^{-1/2}$. The results obtained yield a difference of $T_{cpw} - T_w$ = 8.4 K, as shown in Table 1, and this value agrees with those determined based on GCMC simulations [8,17].

3.3. Calculations at $T < T_t$

Since the determined wetting temperature is lower than the triple point temperature, the adsorbed *Ne* should be liquid in the range of $T_w < T < T_t$. Hence, it is reasonable to perform DFT calculations with the same formalism employed for $T \geq T_t$. Thus, we extrapolated the coexistence curve into this regime and the corresponding parameters comprising $\nu_{id}(T)$, $\tilde{\varepsilon}_{Ne-Ne}(T)$, and $\tilde{\sigma}_{Ne-Ne}(T)$ of the grand canonical functional for Eqs. (2) and (4), were determined. The adsorption isotherms evaluated at T = 22, 23, and 24 K are depicted by dashed curves in Fig. 4a. The overall behavior is similar to that found at $T = T_t$ and shown in Fig. 6, where only the overshoots of the transitions C_i are higher (see Fig. 4a). The results for the excess of the grand potential energy per unit area as a function of the reduced chemical potential are

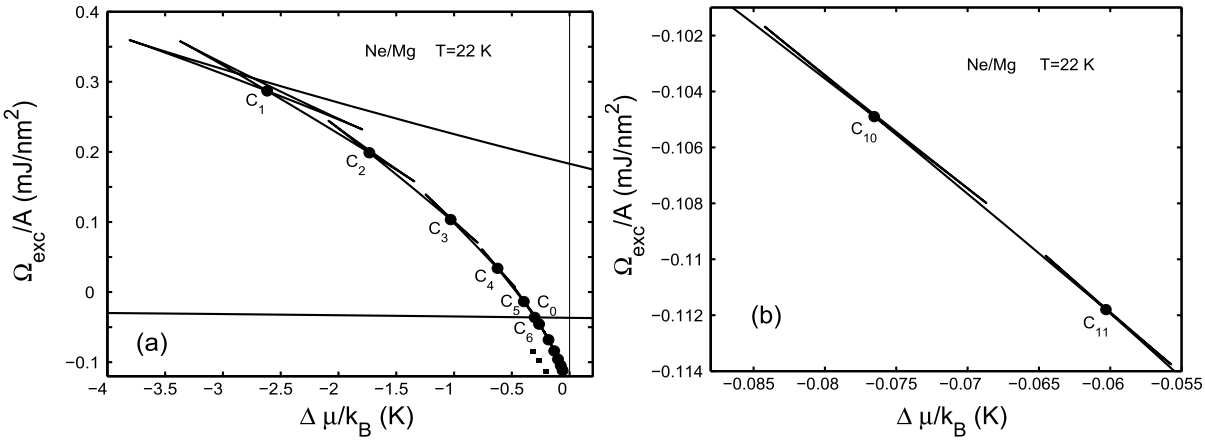

Fig. 13. (a) Enlarged image of the energy curve in Fig. IVb for $T = 22$ K. The point denoted by C_0 is on the main PW line. The meanings of points C_1, C_2, …, C_6 are explained in the text. (b) Enlargements of crossings C_{10} and C_{11}.

shown by the dashed curves in Fig. 4b, where the open circles indicate the crossings that yield the locus of the main PW line. The corresponding values of $\Delta\mu_{pw}(T)$ are given in Fig. 9, where the dashed curve shows the fit of the data for the entire range of $22 \leq T \leq 28$ K to Eq. (18). The determined parameters a_{pw} and T_w are also given in Table 1, where the value obtained for $T_w = 21.0 \pm 0.1$ K is compatible with that produced based on data for $T \geq T_t$. Furthermore, the trend in the coexistent $\Gamma_{\ell,thin}$ and $\Gamma_{\ell,thick}$ at the main PW line follows the expected behavior, as shown in Fig. 10.

We note that there is a high level of similarity between the isotherms shown in Fig. 4a and in Fig. 5 given by [46]. For the *Xe/Li* system. Therefore, it is reasonable to expect that the *Ne/Mg* system should also exhibit a series of PW lines similar to those depicted in Fig. 3c given by Ref. [43] for *Xe/Li*. In fact, the oscillating behavior of $\Delta\mu$ as a function of Γ_ℓ leads to a sequence of first-order layering transitions that yield additional PW lines. The critical points $[T_{cpwi}, \Delta\mu_{cpwi}]$ at which the i-th layering transition terminate are indicated by the squares denoted by C_{pwi} in Fig. 9. These PW lines are only shown up to $i = 8$ because the next ones merge with the $\Delta\mu = 0$ line on the scale used in this figure. As the temperature decreases, all of the lines coalesce into the C_{pw0} curve. All of the critical points C_{pwi} were determined by employing the same procedure used to obtained C_{pw0}. This overall behavior corresponds to that shown in panel (d) of Fig. 1 given by Ref. [7]. We note that the locus of the PW line finishing at C_{pw1} is very short, it appears at $T = 26.35$ K, and at $T = 26$ K it already exhibits a higher Ω_{exc}/A value than that of the main PW line. Therefore, at $T = T_t$, the coverage jump identified by C_1 lies above C_0, as shown in Fig. 6a. At lower temperatures, when T approaches T_w, subsequent crossings $C_{i>1}$ begin to exhibit higher Ω_{exc}/A value than that corresponding to C_0. For instance, as shown in Fig. 13a, the crossings C_1, C_2, …, C_5 already lie above C_0 at $T = 22$ K. In order to illustrate the accuracy of the current calculations, the crossings C_{10} and C_{11} at this temperature are shown in Fig. 13b.

4. Concluding discussion

First, we note that the results obtained using the current DFT calculations for the *Ne/Mg* system differ from those reported by Ref. [15]. These differences can mainly be attributed to two facts: (i) the adsorption potential used by Zhou and Zhang is short range, whereas the potentials used in other studies are long range; and (ii) the augmented DFT formalism employed by Zhou and Zhang does not contain sufficient information about the bulk *Ne*. The adsorption potential $\phi_{ext}(z)$ devised and used by Zhou and Zhang [15] is a short range interaction, which is truncated at $z_{cs} \simeq 3\,\sigma_{Mg-Ne}$. By contrast, the asymptotic expression of the adatom–surface interaction, i.e., at large separation z, given by the $U_{CCZ}(z)$ potential exhibits a long range tail that is proportional to $-1/z^3$. It should be noted that Chapter 2 of [47] presented several approaches that can be used to arrive at the conclusion that an adsorption potential should take the form of $U_{sf}(z \to \infty) \simeq -C_3/z^3$. Moreover, the range of the potentials for atoms over alkaline surfaces is particularly large due to the large decay lengths of the surface electronic charge in these systems. Hence, it appears that the expressions given in Eqs. (1) and (2) by Ref. [15] are not suitable for describing the *Ne/Mg* system. The difference between both adsorption potentials is shown clearly in Fig. 2a. The crucial difference obtained for $\Delta\mu_{pw}/k_B$ at T_t when using the short range $\phi_{ext}(z)$ or the long range $U_{CCZ}(z)$ in the framework of the same DFT is shown in Fig. 2b. Therefore, it is clear that wetting occurs only for $U_{CCZ}(z)$. Moreover, in a very recent study, Evans et al. [48] demonstrated that the nature of the wetting behavior depends on whether the adsorption potential is short or long range. For the *Ne–Ne* interaction, the same MFA given by Eq. (4) was used by Ref. [15] and in the current study. The differences are that Zhou and Zhang used the same values for ε_{Ne-Ne} and σ_{Ne-Ne} at all temperatures and the LJ potential was truncated at 4σ, whereas in our calculations, we assumed that these strength and size parameters are functions of T and that the LJ potential is not truncated. The DFT calculations conducted by Zhou and Zhang's led to an important difference between the asymptotic pressure for very thick films at a given T and the corresponding experimental saturated vapor pressure $P_0(T)$. By contrast, we showed that in the case of the current DFT formalism, even for $\phi_{ext}(z)$, the asymptotic pressure approaches $P_0(T)$, although from above (see Fig. 7).

In fact, in the case of the current DFT, in addition to fitting the LJ parameters $\tilde{\varepsilon}_{Ne--Ne}(T)$ and $\tilde{\sigma}_{Ne-Ne}(T)$ in order to reproduce the data in the liquid-vapor coexistence curve quoted in Table III given by Ref. [40], we successfully checked the prediction of the liquid–vapor surface tension at saturation given by the formalism as a function of T [9]. Moreover, this DFT was employed to analyze the wetting properties of *Ne* adsorbed on *Cs, Rb, K, Li,* and *Mg*. This sequence of substrates exhibit increasing attractive strength, which leads to a variety of wetting situations along the entire range of temperatures spanned from the triple point temperature T_t up to the critical point temperature T_c. These calculations suggest nonwetting for *Ne/Cs* and a wetting temperature close to T_c for *Ne/Rb* (both results are in agreement with the experimental findings [13]).

Furthermore, in the present study, we extended the DFT calculations below T_t. The results obtained for temperatures in the regime of $T_w < T < T_t$ exhibited trends that were compatible with those exhibited for $T \geq T_t$. In addition, we proposed a novel procedure for determining T_{cpw}, which is particularly useful for moderately strong adsorption potentials. Our new calculations facilitated very accurate evaluations of both T_w and T_{cpw}, which yielded values that are compatible with the

GCMC estimates given by Refs. [8,17]. The range of temperatures obtained for the wetting behavior of *Ne/Mg* have not been measured previously, so these are predictions. Finally, we should stress that some additional interesting features were determined by employing the arc-length continuation algorithm to analyze the adsorption isotherms. For instance, at $T \lesssim T_t$, after the main PW jump, the film grows exhibiting a series of coalescent PW lines, as expected for moderately strongly attractive substrates.

Acknowledgements

This study was supported partly by the Ministry of Science and Technological Innovations of Argentina through Grant No. CONICET PIP-112-2015-01-00417.

References

[1] P.G. de Gennes, Wetting: statics and dynamics, Rev. Mod. Phys. 57 (1985) 827.
[2] P.G. de Gennes, F. Brochard-Wyart, D. Quéré, Capillarity and Wetting Phenomena, Springer, Berlin (Germany), 2003.
[3] Special Issue: Wetting, Spreading and filling, guest, in: M.S. Petersen, M.W. Cole (Eds.), J. Low Temp. Phys, vol 157, 2009, p. 75.
[4] A. Kayal, A. Chandra, J. Chem. Phys. 143 (2015) 224708.
[5] H.H. Wei, Y.C. Li, Phys. Rev. E 94 (2016) 012501.
[6] R. Pandit, M. Schick, M. Wortis, Phys. Rev. B 26 (1982) 5112 (citations therein).
[7] R. Pandit, M.E. Fisher, Phys. Rev. Lett. 51 (1983) 1772.
[8] S. Curtarolo, G. Stan, M.J. Bojan, M.W. Cole, W.A. Steele, Phys. Rev. E 61 (2000) 1670.
[9] S.A. Sartarelli, L. Szybisz, I. Urrutia, Phys. Rev. E 79 (2009) 011603.
[10] C. Ebner, W.F. Saam, Phys. Rev. Lett. 38 (1977) 1486.
[11] L. Szybisz, Phys. Rev. B 67 (2003) 132505.
[12] E. Cheng, G. Mistura, H.C. Lee, M.H.W. Chan, M.W. Cole, C. Carraro, W.F. Saam, F. Toigo, Phys. Rev. Lett. 70 (1993) 1854.
[13] G. Mistura, H.C. Lee, M.H.W. Chan, J. Low Temp. Phys. 96 (1994) 221.
[14] D. Ross, P. Taborek, J.E. Rutledge, Phys. Rev. B 58 (1998) R4274.
[15] S. Zhou, M. Zhang, J. Phys. Chem. Solid. 103 (2017) 123.
[16] S. Zhou, Commun. Theor. Phys. 54 (2010) 1023.
[17] M.J. Bojan, G. Stan, S. Curtarolo, W.A. Steele, M.W. Cole, Phys. Rev. E 59 (1999) 864 M. J. Bojan, M. W. Cole, I. K. Johnson, W. A. Steele, Q. Wang, J. Low Temp. Phys. 110 (1998) 653.
[18] A. Chizmeshya, M.W. Cole, E. Zaremba, J. Low Temp. Phys. 110 (1998) 677.
[19] R. Evans, Density functionals in the theory of nonuniform fluids, in: D. Henderson (Ed.), Fundamentals of Inhomogeneous Fluids, Decker, New York, 1992(Chapter 3).
[20] F. Ancilotto, S. Curtarolo, F. Toigo, M.W. Cole, Phys. Rev. Lett. 87 (2001) 206103.
[21] E. Cheng, M.W. Cole, W.F. Saam, J. Treiner, Phys. Rev. B 48 (1993) 18215.
[22] E. Kierlik, M.L. Rosinberg, Phys. Rev. 42 (1990) 3382.
[23] Y. Rosenfeld, Phys. Rev. Lett. 63 (1989) 980.
[24] J.D. Weeks, D. Chandler, H.C. Andersen, J. Chem. Phys. 54 (1971) 5237.
[25] F. Ancilotto, F. Toigo, Phys. Rev. B 60 (1999) 9019.
[26] E. Bruno, C. Caccamo, P. Tarazona, Phys. Rev. 35 (1987) 1210.
[27] H. Hansen-Goos, J. Phys. Condens. Matter 28 (2016) 240001.
[28] P. Tarazona, Phys. Rev. Lett. 84 (2000) 694.
[29] B. Peng, Y.-X. Yu, J. Phys. Chem. B 112 (2008) 15407.
[30] J.K. Johnson, J.A. Zollweg, K.E. Gubbins, Mol. Phys. 78 (1993) 591.
[31] A. Nasehzadeh, M. Mohseni, K. Azizi, J. Mol. Struct. 589–590 (2002) 329.
[32] A. Kh, Al Matar, A.H. Togby, I.A. Suleiman, Mol. Simulat. 34 (2008) 289.
[33] M. Damyanova, E. Balabanova, U. Hohlm, J. Phys. Conf. Series 514 (2014) 012055.
[34] K.T. Tang, J.P. Toennies, Surf. Sci. 279 (1992) L203.
[35] F. Ricca, Nuovo Cim. Supl. V (1967) 339.
[36] W.A. Steele, Interaccion of Gases with Solid Surfaces, Pergamon, Oxford, 1974.
[37] G.A. Mansoori, N.F. Carnahan, K.E. Starling, T.W. Leland Jr., J. Chem. Phys. 54 (1971) 1523.
[38] N.F. Carnahan, K.E. Starling, J. Chem. Phys. 51 (1969) 635.
[39] R. Roth, R. Evans, A. Lang, G. Kahl, J. Phys. Condens. Matter 14 (2002) 12063.
[40] V.A. Rabinovich, A.A. Vasserman, V.I. Nedostup, L.S. Veksler, Thermophysical Properties of Neon, Argon, Krypton and Xenon (Hemisphere, Washington, DC, (1988).
[41] E.A. Guggenheim, J. Chem. Phys. 13 (1945) 253.
[42] J. Vrabec, G.K. Kedia, G. Fuchs, H. Hasse, Mol. Phys. 104 (2006) 1509.
[43] L. Szybisz, S.A. Sartarelli, AIP Adv. 1 (2011) 042146.
[44] S.A. Sartarelli, L. Szybisz, J. Phys. Chem. B 117 (2013) 6256.
[45] R. Evans, J. Phys. Condens. Matter 2 (1990) 8989.
[46] S.A. Sartarelli, L. Szybisz, Physica a 407 (2012) 3278.
[47] L.W. Bruch, M.W. Cole, E. Zaremba, Physical Adsorption: Forces and Phenomena, Clarendon, Oxford, 1997.
[48] R. Evans, M.C. Stewart, N.B. Wilding, J. Chem, Phys. Nor. 147 (2017) 044701.